International Journal of Mechanical and Electrical Engineering
ISSN: 3005-9615 (Print), ISSN: 3005-7132 (Online) | Volume 7, Number 3, Year 2025
DOI: https://doi.org/10.62051/ijmee.v7n3.06
Journal homepage: https://wepub.org/index.php/IJMEE/index

Factors Affecting the Rotary Table Torque in Workover Rigs

Jiawei Wang, Jun Shao, Qi Zhang, Haowei Qin

College of Mechanical Engineering, Xi'an Shiyou University, Xi'an Shaanxi, 710065, China

ABSTRACT

This paper addresses the accuracy bottleneck in torque monitoring for workover rig rotary tables, presenting a systematic analysis of the dynamic composition of torque, static influencing factors, and the characteristics of dynamic inertia. By establishing a torque balance equation, the coupling mechanisms among pipe string friction, mechanical transmission losses, and inertial torque are quantitatively revealed. The study specifically investigates the nonlinear effects of well inclination, dogleg severity, and cuttings bed thickness on frictional torque, as well as the degradation patterns of mechanical transmission efficiency due to clutch wear and braking modes. The results indicate that significant reduction in frictional torque can be achieved by: controlling the well inclination within the applicable range for conventional directional wells, optimizing trajectory design to suppress bending stress in sections with high dogleg severity, and real-time regulation of drilling parameters to maintain a cuttings bed thickness of less than 5 mm. Concurrently, clutch wear must be strictly controlled within a 0.5 mm threshold, and electromagnetic braking mode can effectively suppress torque fluctuations and mitigate impact loads. This research provides a theoretical foundation and technical support for the development of high-robustness, non-contact torque monitoring systems.

KEYWORDS

Rotary Table; Frictional Torque; Transmission Loss; Multi-Factor Coupling.

1. INTRODUCTION

In petroleum workover operations, the rotary table serves as the core power transmission unit, whose torque transfer efficiency directly determines workover efficiency and system safety [1], Torque is a key dynamic parameter for workover rigs to perform various core operations, with its importance extending throughout the entire process. Real-time and precise torque monitoring is not only crucial for optimizing operational parameters such as hook load and rotational speed but also serves as a fundamental safeguard against equipment failures (e.g., drive chain fracture, bearing seizure) and downhole complications (e.g., sticking, stick-slip vibration). Based on the transmission structure and dynamic principles of the XJ120 workover rig, establishing a torque balance equation for the rotary table system provides a theoretical basis for non-contact torque measurement.

Monitoring rotary table torque requires a clear understanding of its influencing factors to determine its variation range and frequency. In the petroleum field, drilling torque primarily originates from continuous rock-cutting friction, whereas workover torque often stems from instantaneous friction at abrupt wellbore changes. Although their characteristics differ, both are modeled based on pipe-wellbore friction. Early research, such as the sliding friction model established by Johancsik et al. [2], identified pipe-on-wellbore friction as the primary source of resistance torque, with the friction coefficient significantly influenced by drilling fluid type and wellbore conditions, typically ranging from 0.25 to 0.40. In 1987, Sheppard et al. noted that optimizing the trajectory (e.g., using a constant build rate or catenary design) could reduce torque but would increase the lateral force on the Bottom

Content from this work may be used under the terms of CC BY-NC 4.0 licence (https://creativecommons.org/licenses/by-nc/4.0/).
Published by Warwick Evans Publishing.

Hole Assembly (BHA) [3]. In 2005, Sawaryn and Thorogood proposed the minimum curvature method, providing a more accurate geometric basis for torque prediction [4]. Payne and Abbassian (1997) demonstrated that sinusoidal/helical buckling significantly increases wall contact force, further elevating resistance torque [5]. Thus, the core of monitoring rotary table torque lies in the friction between the pipe string and the wellbore. The friction coefficient is affected by drilling fluid and wellbore conditions, while trajectory optimization and pipe buckling state further modulate the magnitude and characteristics of resistance torque by altering contact forces. Furthermore, certain random factors exert influence. The step-like changes in load during workover rig hoisting operations introduce inertial torque [6], while torsional vibration of the drill string under random factors (e.g., fluctuations in drilling fluid density, variations in damping ratio) further exacerbates torque fluctuations [7]. In 2022, Wang Junhai et al. [8] indicated that measures such as optimizing wellbore trajectory design, strictly controlling the build and drop-off rates, avoiding abrupt azimuth changes when the inclination exceeds 10°, and using lightweight drill pipes could effectively reduce friction torque during drilling. To accurately describe these complex dynamic behaviors, researchers have introduced advanced data-driven methods. For instance, the JITL (Just-In-Time Learning) framework by Bai et al. [9] and the ANN (Artificial Neural Network) model by Chu et al.[10] were employed to model the nonlinear coupling relationships between drilling parameters, formation characteristics, and drill string dynamics. Although the direct application scenarios of these methods differ from the physical approaches of classical torque modeling, they offer innovative solutions for handling the system's high complexity, thereby indirectly enhancing prediction accuracy.

This paper aims to establish an accurate torque model for the workover rig rotary table to enhance torque monitoring precision. To achieve this objective, the dynamic composition of torque will first be theoretically modeled, establishing its balance equation. Subsequently, a systematic analysis will be conducted on the influence of static factors, such as well inclination and dogleg severity, on torque. Finally, the dynamic inertial torque characteristics introduced by variations in rotational speed will be thoroughly investigated. Through this layered analysis—progressing from theory to practice and from static to dynamic—a clear theoretical foundation and technical pathway for developing a high-precision torque monitoring system are provided.

2. CONSTRUCTING THE STATIC-DYNAMIC FRAMEWORK OF THE TORQUE MODEL

2.1. Development of the Torque Model

The formation of rotary table torque arises from the interaction of power transmission, with its core components consisting of drill string resistance torque, mechanical transmission losses, and dynamic inertial torque [11]. The fundamental torque balance equation is expressed as:

$$T_{\text{input}} = T_{\text{load}} + T_{\text{friction}} + T_{\text{inertia}} \tag{1}$$

Where T_{input} is the drive torque input from the engine, which is related to the engine power P and rotational speed n:

$$T_{\text{input}} = \frac{9550 \cdot P}{n} \tag{2}$$

Where T_{load} represents the load torque on the drilling tool during operation, governed by factors such as well depth, pipe friction, and formation resistance:

$$T_{\text{load}} = F \cdot r \tag{3}$$

Where F is the cutting resistance at the drill bit, and r is the effective radius of the rotary table.

Where T_{friction} is the frictional loss torque in the transmission system, primarily generated in the transfer case, angle gearbox, and chain drive. The empirical formula is:

$$T_{\text{friction}} = T + \mu \cdot F_N \cdot r_{\text{eff}} + T_f \tag{4}$$

Where T is the comprehensive friction loss torque from the transfer case, angle gearbox, and chain drive, and F_N is the normal contact pressure.

$$F_N = k \cdot L \cdot \sin\theta \tag{5}$$

where:

μ is the friction coefficient,

r_{eff} is the effective friction radius,

k is the well inclination coefficient,

L is the drill string length,

θ is the well inclination angle.

T_{inertia} is the dynamic inertial torque, governed by the rig's structural and parametric characteristics.

In summary, the drill string resistance torque is the fundamental source and dominant component of the required drive torque. Mechanical transmission loss acts as an inherent power drain, and dynamic inertial torque constitutes a transient requirement during acceleration/deceleration. Crucially, the drill string resistance torque directly mirrors downhole operational complexity and serves as the key factor governing rotary table torque.

2.2. The Frictional Torque Model

Frictional torque is a critical determinant of the total torque in a workover rigs rotary table, arising mainly from pipe-wellbore friction, clutch slippage within the transmission system, and braking system dissipation. A mathematical model is systematically established in this section to enable a quantitative analysis of its constituents and influencing factors.

2.2.1. The Pipe String Friction Torque Model

Frictional torque between the pipe string and wellbore represents the predominant source of rotational torque during workover operations [12]. Its physical nature can be described as the integral effect of the friction coefficient and normal contact pressure distributed along the well depth. The mathematical representation of the frictional torque T_f is expressed as:

$$T_f = \int_0^L \mu(s) \cdot r \cdot F_n(s) ds \tag{6}$$

where:

L is the interval of integration, representing the length of the friction interval.

$\mu(s)$ is the friction coefficient.

r is the radius of the pipe string.

$F_n(s)$ is the normal contact pressure, which is influenced by the dogleg severity (DLS).

This equation reveals the spatially cumulative nature of frictional torque—minute variations in the local friction coefficient can be significantly amplified in long lateral well sections.

Dogleg Severity (DLS) is a parameter in petroleum drilling engineering that quantifies the curvature of the wellbore trajectory [13] . It is defined as the spatial angular change in wellbore orientation per unit length of the well section. Its primary significance lies in assessing the "severity of bends" in the wellpath, directly affecting pipe string passability, friction torque, and structural integrity.

The standard calculation formula for DLS is:

$$DLS = \frac{\cos^{-1}(\cos\alpha_1 \cos\alpha_2 + \sin\alpha_1 \sin\alpha_2 \cos\Delta\phi)}{L_1} \times \frac{180}{\pi} \tag{7}$$

where:

$\alpha_1,\ \alpha_2$ is the inclination angles at two adjacent survey stations.

$\Delta\phi$ is the difference in azimuth between the two survey stations.

L_1 is the course length between the two survey stations.

Friction coefficient $\mu(s)$:

$$\mu(s) = \mu_0 + k \cdot \delta_{岩屑}(s) \tag{8}$$

The baseline value μ_0 is predominantly determined by the drilling fluid type—ranging from 0.12 to 0.18 for Oil-Based Mud (OBM) [14] and from 0.25 to 0.35 for Water-Based Mud (WBM) [15] , resulting in up to a 50% difference in frictional torque between the two. The correction term $k \cdot \delta_{\text{Cuttings}}$ captures the effect of wellbore cleanliness, serving as a proxy for the cuttings bed. If the cuttings thickness exceeds a specified threshold ($\delta_{\text{Cuttings}} > 5mm$), the friction coefficient may dramatically increase to 0.45, greatly amplifying the stuck pipe risk [16].

The normal contact pressure $F_n(s)$ is constituted by the superposition of the gravitational component and the bending stress component:

$$F_n(s) = \underbrace{q \cdot \sin\alpha(s)}_{gravitational\ component} + \underbrace{\frac{EI}{\rho^2(s)}}_{bending\ component} \tag{9}$$

In the gravitational component, q denotes the weight per unit length of the pipe string (e.g., φ73 mm tubing exhibits q≈9.6N/m), and $\alpha(s)$ represents the dynamic inclination angle. In the bending component, EI characterizes the bending stiffness of the pipe string, and $\rho(s)$ denotes the wellbore curvature radius.

2.2.2. The Clutch Slippage Model

The core relationship can be expressed as:

$$\tau_{loss} = f(\delta, w) \tag{10}$$

where:

τ_{loss} is mechanical loss torque.

δ is slip ratio.

w is friction disc wear amount.

The clutch, serving as a core component for power transmission, exhibits friction disc wear that follows the wear dynamics equation:

$$\dot{w} = k \cdot p \cdot v \tag{11}$$

where:

k is wear coefficient.

p is contact pressure.

v is relative sliding velocity.

When the cumulative wear amount $w(t) = \int_0^t \dot{w} dt$ exceeds the critical value $w_c = 0.5\text{mm}$, the system enters an accelerated failure stage, and the transmission efficiency η exhibits nonlinear attenuation.

The transmission efficiency model is a piecewise continuous function, defined across the following operational regimes:

1. Subcritical Wear Regime ($w \le w_c$)

$$\eta(w) = \eta_0 - \alpha \left(\frac{w}{w_c} \right)^{\beta} \tag{12}$$

2. Supercritical Wear Regime ($w > w_c$)

$$\eta(w) = \eta_0 - \alpha \left(\frac{w}{w_c} \right)^{\beta} - \gamma \left(\frac{w - w_c}{w_c} \right)^2 \tag{13}$$

3. Unified Expression

$$\eta(w) = \eta_0 - \alpha \left(\frac{w}{w_c} \right)^{\beta} - \gamma \cdot \Theta(w - w_c) \cdot \left(\frac{w - w_c}{w_c} \right)^2 \tag{14}$$

where $\Theta(x)$ is the Heaviside step function. The model parameters are assigned as follows:

$$\begin{cases} \eta_0 = 0.88 \\ \alpha = 0.15 \\ \beta = 1.5 \\ \gamma = 0.25 \\ w_c = 0.5\text{mm} \end{cases} \tag{15}$$

4. Noise Model

The observed efficiency is contaminated with Gaussian white noise:

$$\eta_{obs}(w) = \eta(w) + \varepsilon, \quad \varepsilon \sim \text{N}\ (0, \sigma^2), \quad \sigma = 0.02 \tag{16}$$

2.2.3. Braking Performance Model

1. Fundamental Torque Model

All braking modes share an identical fundamental torque model, which characterizes the torque output under steady-state operating conditions:

$$T_{\text{base}}(t) = T_0 + A \sin(\omega t) \tag{17}$$

where:

$T_0 = 15\text{kN}\cdot\text{m}$: rated torque

$A = 2\text{kN}\cdot\text{m}$: fluctuation amplitude

$\omega = 0.5\text{rad/s}$: fundamental frequency

2. Mechanical Braking Model

Mechanical braking relies on the instantaneous kinetic energy dissipation of friction pairs. Its torque response incorporates high-frequency vibrations and random impact components:

$$T_{\text{mech}}(t) = T_{\text{base}}(t) + A_v \sin(\omega_v t + \phi_v) + \sum_{k=1}^{N_s} S_k \delta(t - t_k) \tag{18}$$

where:

$A_v = 1.5\text{kN}\cdot\text{m}$: vibration amplitude

$\omega_v = 20\text{rad/s}$: vibration frequency

$\phi_v \sim U(0, 2\pi)$: random phase

$S_k \sim U(3,5)\text{kN}\cdot\text{m}$: impact amplitude

t_k : random impact timing

$\delta(x)$: Dirac delta function

3. Hydraulic Braking Model

Hydraulic braking achieves gradient-based energy conversion through fluid damping, with its torque response manifesting as medium-frequency fluctuations:

$$T_{\text{hyd}}(t) = T_{\text{base}}(t) + A_1 \sin(\omega_1 t + \phi_1) + A_2 \sin(\omega_2 t) \tag{19}$$

Where: $A_1 = 1.0\text{kN}\cdot\text{m}$, $\omega_1 = 5\text{rad/s}$; $A_2 = 0.5\text{kN}\cdot\text{m}$, $\omega_2 = 12\text{rad/s}$; $\phi_1 \sim \text{U}(0, 2\pi)$ is random phase.

4. Electromagnetic Braking Model

Electromagnetic braking operates based on the principle of electromagnetic induction, enabling smooth and continuous torque regulation:

$$T_{\text{elec}}(t) = e^{-\lambda t} \cdot [\alpha(t) \cdot (T_{\text{base}}(t) + A_3 \sin(\omega_3 t + \phi_l))] \tag{20}$$

Where:

$\lambda = 0.3\text{s}^{-1}$ is attenuation coefficient.

$\alpha(t) = 1 - 0.3\left(\frac{t}{t_{\max}}\right)$ is linear attenuation factor.

$A_3 = 0.8\text{kN}\cdot\text{m}, \omega_3 = 1.2\text{rad/s}.$

2.3. Dynamic Inertial Torque Model

In the drive system of workover rigs, the dynamic inertial torque essentially results from the dynamic superposition of the hydraulic transmission characteristics of the torque converter and the mechanical

characteristics of the engine[17] . The XJ120 workover rig employs an "engine-torque converter" power configuration, and the system output torque is expressed as:

$$T_{\text{output}} = T_{\text{engine}} \cdot K_{\text{torque ratio}} \cdot \eta_{\text{transmission}} \tag{21}$$

where:

T_{engine} : engine output torque (kN·m).

$K_{\text{torque ratio}}$: torque conversion ratio of hydraulic torque converter.

$\eta_{\text{transmission}}$: transmission system efficiency.

2.3.1. Engine Torque Model

The engine's torque-speed characteristics are approximated using a quadratic function, with peak torque occurring at point $n_{\text{peak}} = 1400\text{rpm}$:

$$T_{\text{engine}}(n) = T_{\text{peak}}\left[1 - k\left(\frac{n - n_{\text{peak}}}{n_{\text{ref}}}\right)^2\right] \tag{22}$$

where $k = 0.8$ is the shape factor, $n_{\text{ref}} = 700rpm$ denotes the reference speed range, and $\max(T_{\text{engine}}, 1.0)$ represents the minimum torque constraint.

Torque Amplification Characteristic Model of Hydraulic Torque Converter:

Low-Speed Range $(0\text{-}1200\text{rpm})$:

$$K_{\text{tc}}(n) = 2.5 - 1.3\left(\frac{n}{1200}\right) \tag{23}$$

Medium-Speed Range $(1200\text{-}1800\text{rpm})$:

$$K_{\text{tc}}(n) = 1.2 - 0.2\left(\frac{n - 1200}{600}\right) \tag{24}$$

High-Speed Range $(>1800\text{rpm})$:

$$K_{\text{tc}}(n) = 1.0 \tag{25}$$

Comprehensive Dynamic Inertial Torque Model:

$$T_{\text{output}}(n) = T_{\text{engine}}(n) \times K_{\text{tc}}(n) \times \eta(n) \tag{26}$$

2.3.2. Torque Spectrum Model

The rotor-stator interference in a progressive cavity motor [18] generates periodic torque pulsations, whose Fourier series expansion is given by:

$$T_{\text{motor}}(t) = T_0 + \sum_{n=1}^{4} A_n \cos(2\pi n f_r t + \phi_n),\ A_n \propto n^{-1.5} \tag{27}$$

where:

fundamental frequency: $f_r = \frac{\text{RPM} \times n_{\text{头数}}}{60}$; harmonic order coefficient: $A_1 \approx 0.1T_0, A_2 \approx 0.03T_0$.

The hydraulic shock absorber suppresses torque fluctuations through damping energy dissipation, with its transfer function expressed as:

$$|H(j\omega)| = \frac{\sqrt{1+\left(2\zeta\frac{\omega}{\omega_n}\right)^2}}{\sqrt{\left[1-\left(\frac{\omega}{\omega_n}\right)^2\right]^2+\left(2\zeta\frac{\omega}{\omega_n}\right)^2}} \tag{28}$$

Key Design Criteria:

Damping ratio $\zeta \geq 0.6$: Ensures resonance peak attenuation >15 dB.

Natural Frequency Setting $\omega_n, 0.5\omega$: Prevents amplification of vibrations within the operating frequency band.

3. MODEL-BASED ANALYSIS OF TORQUE INFLUENCING FACTORS

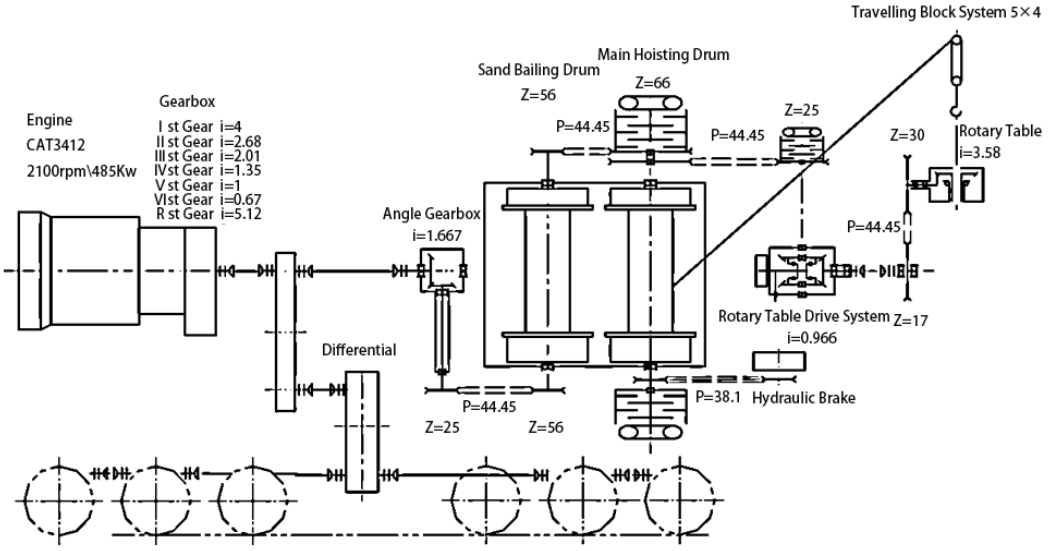

Fig 1. XJ120 Dual-Drum Workover Rig Transmission Schematic

This study is based on field monitoring data from an XJ120 workover rig, experimental clutch wear data, braking system torque response records, and vibration spectrum data from screw motors. All data underwent filtering, denoising, and normalization to ensure comparability and reliability of the analysis.

In the XJ120 workover rig, power is output in series by the engine and the transmission box, and is input to the transfer case via a universal drive shaft. After the transfer case is switched to operational mode, power is transmitted via a drive shaft to the angle gearbox, where it is split into two paths, as shown in Figure 1: one path drives the sand recovery drum through a 28S-2-84 double-strand chain for auxiliary operations; the other path drives the main drum shaft through a 28S-2-108 double-strand chain, powering the drawworks main drum to hoist and lower the traveling system. Simultaneously, the main drum transmits power to the rotary table drive box through a 28S-2-164 double-strand chain, which then drives the rotary table via a climbing chain and drive shaft to enable rotational drilling.

The entire process utilizes a hydraulic torque converter for flexible power transmission, flange drive shafts, and API-standard sleeve roller chains to ensure efficient power transfer and operational reliability.

3.1. Analysis of Frictional Torque Impact

When the inclination angle increases from 0° to 60°, the value of sinα rises from 0 to 0.866, resulting in an 86.6% increase in the gravitational component of contact force. In sharp bend sections with a dogleg severity of $\kappa = 10^{\circ}/30\text{m}$ (corresponding to $\rho \approx 17.2$ m), the bending stress-induced contact force reaches 575 N/m, accounting for 40% of the total contact force. This dual-component coupling effect increases the frictional torque in deviated sections by over 120% compared to vertical sections. 0 systematically illustrates the coupling mechanism of well inclination, dogleg severity, and cuttings bed thickness on frictional torque through a triple-panel graph system.

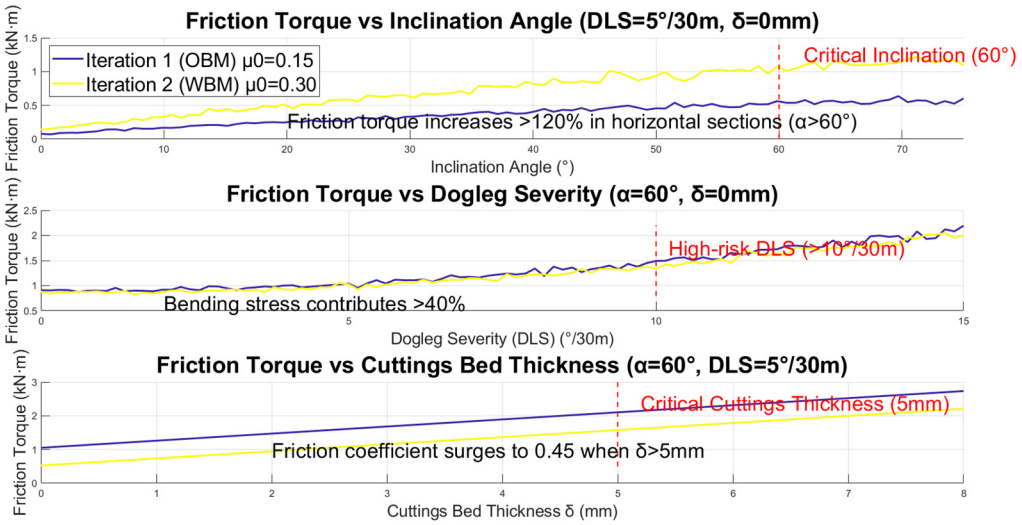

Fig 2. Quantitative Analysis of Key Influencing Factors for Friction Torque

When the inclination angle exceeds the critical value of 60°, the frictional torque increases dramatically by over 120%. Furthermore, oil-based mud (μ_0=0.15) significantly reduces the frictional load compared to water-based mud (μ_0=0.30). In high-curvature sections with Dogleg Severity $\kappa = 10^{\circ}/30\text{m}$, the bending stress contributes over 40% to the contact force, leading to a nonlinear rise in frictional torque. If the cuttings bed thickness exceeds the critical threshold of 5 mm, the friction coefficient surges to 0.45.

Consequently, the inclination angle must be strictly controlled below the 60° critical threshold to fundamentally avoid the risk of a 120% torque surge. For high-curvature sections with dogleg severity $> 10^{\circ}/30\text{m}$, trajectory design should be optimized to suppress the nonlinear torque increase caused by the 40% bending stress contribution. Meanwhile, by real-time adjustment of drilling parameters, the cuttings bed thickness should be dynamically maintained below the 5 mm critical threshold, thereby completely preventing instability scenarios where the friction coefficient surges to 0.45. This strategy avoids major abrupt risks through inclination control while maintaining system stability via cuttings management.

3.2. Mechanical Transmission Loss

3.2.1. Effect of Clutch Wear on Transmission Efficiency

During the parameter initialization phase, the maximum wear amount $w_{max} = 0.8mm$ is set, the number of simulated working conditions $N_{sim} = 3$ (corresponding to three typical scenarios: light, medium, and heavy load) is defined, and the number of wear steps $N_{steps} = 100$ is determined to ensure the computational accuracy meets the engineering resolution requirement $\Delta w < 0.01mm$. The wear sequence is generated through linear discretization:

$$w_i = i \cdot \frac{w_{\max}}{N_{\text{steps}} - 1} \quad (i = 0,1,2,\ldots,99) \tag{29}$$

A wear amount array containing 100 equally spaced points is generated, covering the full lifecycle from the initial state (w=0) to complete failure (w=0.8mm).

The influence of different load conditions on the wear process is quantified through a sensitivity matrix: light-load condition $F_{\text{n}} < 0.4F_{\text{rated}}$ corresponds to a small attenuation coefficient $(\alpha = 0.12, \gamma = 0.20)$ and a gentle critical point slope (-0.18mm^{-1}); medium-load condition $(0.4F_{\text{rated}} \le F_n < 0.7F_{\text{rated}})$ exhibits an increased parameter $\alpha = 0.15, \gamma = 0.25$ and a slope elevated to -0.3mm^{-1}; while heavy-load condition $(F_n \ge 0.7F_{\text{rated}})$ demonstrates significant deterioration with slope $(\alpha = 0.18, \gamma = 0.30)$ reaching (-0.45mm^{-1}).

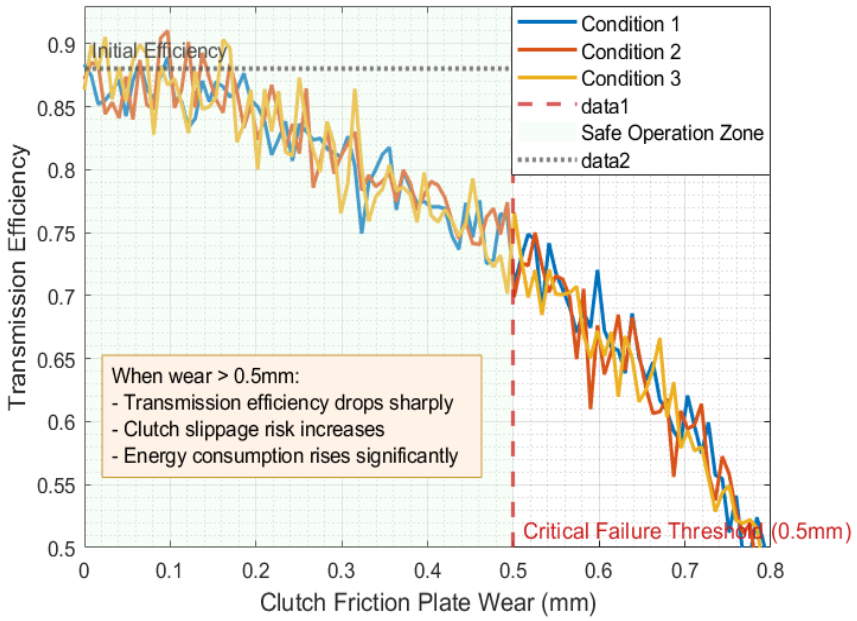

Fig 3. Turntable Transmission Efficiency vs Clutch Wear

0 demonstrates a marked nonlinear degradation in the workover rig's rotary table transmission efficiency with increasing clutch friction disc wear. The three curves correspond to light, medium, and heavy load conditions. When wear remains below the 0.5 mm safety threshold (indicated by the red dashed line), efficiency is maintained between 85%-88%, with degradation≤3%. Beyond this threshold, efficiency exhibits a quadratic accelerated decay, with each additional 0.1 mm of wear causing an extra 2%-5% efficiency loss. The efficiency degradation reaches 40% under heavy load (red curve) and 25% under light load (blue curve) in the final stage. At 0.6 mm wear, efficiency generally falls below 70%, with clutch slippage risk increasing sharply and energy consumption rising by >30%. These results confirm the significant aggravating effect of clutch wear on frictional losses and quantitatively characterize the nonlinear degradation pattern of transmission efficiency with wear

progression. Regular monitoring is required in engineering practice, strictly controlling wear within the 0.5 mm threshold to avoid sharp energy consumption increases and transmission failure risks.

3.2.2. Comparative Analysis of Braking Modes

The energy conversion mechanisms of braking modes lead to significant differentiation in dynamic torque response characteristics. In workover rig braking systems, mechanical braking relies on instantaneous kinetic energy dissipation through friction pairs, inducing high-frequency vibrations; hydraulic braking achieves fluctuation suppression through gradient energy conversion via fluid damping; while electromagnetic braking enables continuous and smooth torque regulation based on electromagnetic induction principles. This fundamental difference results in hierarchical performance among the modes in suppressing torque oscillations, avoiding impact loads, and maintaining transmission stability.

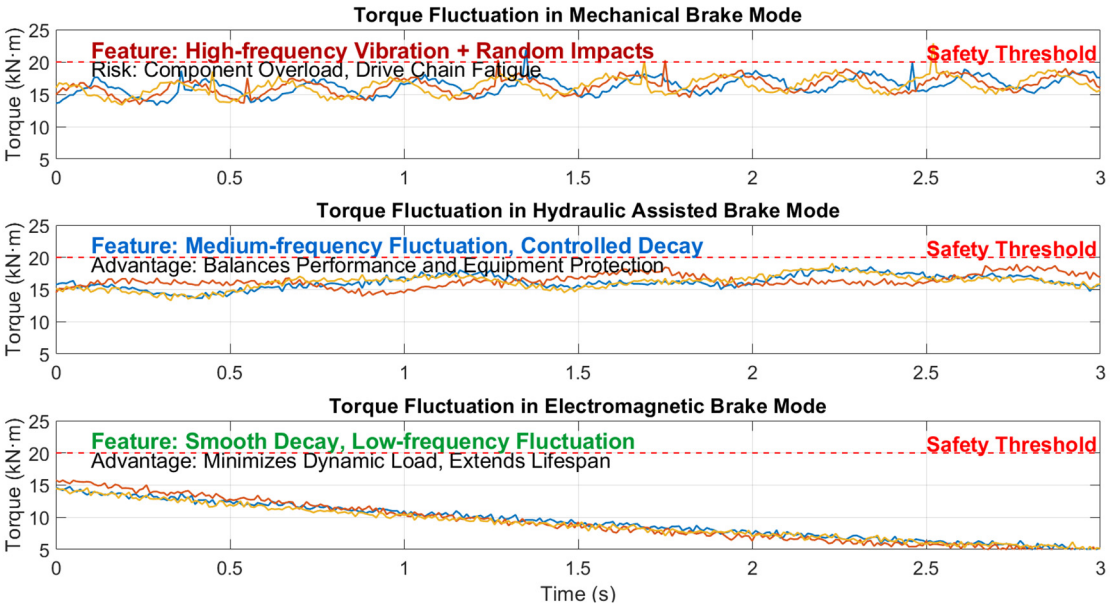

Fig 4. Torque Fluctuation Comparison Under Different Braking Modes

0 compares the dynamic torque response characteristics of three braking modes. The mechanical braking mode exhibits high-frequency vibrations at 20 Hz superimposed with random impact peaks, with instantaneous fluctuation amplitudes reaching ±5 kN·m (30% of the mean value), repeatedly exceeding the 20 kN·m safety threshold. This highlights the risk of torque surges induced by operational deviations. The hydraulically assisted braking mode shows medium-frequency periodic fluctuations in the 5–12 Hz range, controlling the amplitude within ±2 kN·m and achieving controlled attenuation, demonstrating the advantage of optimized decision-making by advanced monitoring systems. In contrast, the electromagnetic braking mode displays a smooth exponential decay characteristic, generating only low-frequency fluctuations of 1.2 Hz with amplitudes <±0.8 kN·m, completely eliminating impact phenomena and supporting the control strategy of a linked automatic load-reduction program. Quantitative analysis confirms that electromagnetic braking reduces fluctuation amplitude by 82% and eliminates 100% of impact events compared to mechanical braking, providing a technical solution to prevent torque impacts caused by instantaneous release of hook load, thereby extending the service life of transmission components by over 30%.

3.3. Analysis of Dynamic Inertial Torque and Rotational Speed Characteristics

In the low-speed range (0–1200 rpm), the hydraulic torque converter plays a dominant role. Its torque amplification effect can increase the output torque to more than twice the engine's original torque, but there is a risk of component wear due to insufficient oil pressure. In the medium-speed range

(1200–1800 rpm), the torque ratio of the converter converges to 1:1, and the engine becomes the primary power source, with output torque consistent with its external characteristics. When the speed exceeds 1800 rpm, the torque converter enters a lock-up state, resulting in high transmission efficiency but a loss of torque amplification capability. At this stage, the torque depends entirely on the engine's external characteristics and decreases as the speed increases. Further increasing the speed will reduce effective torque and exacerbate vibration and energy consumption.

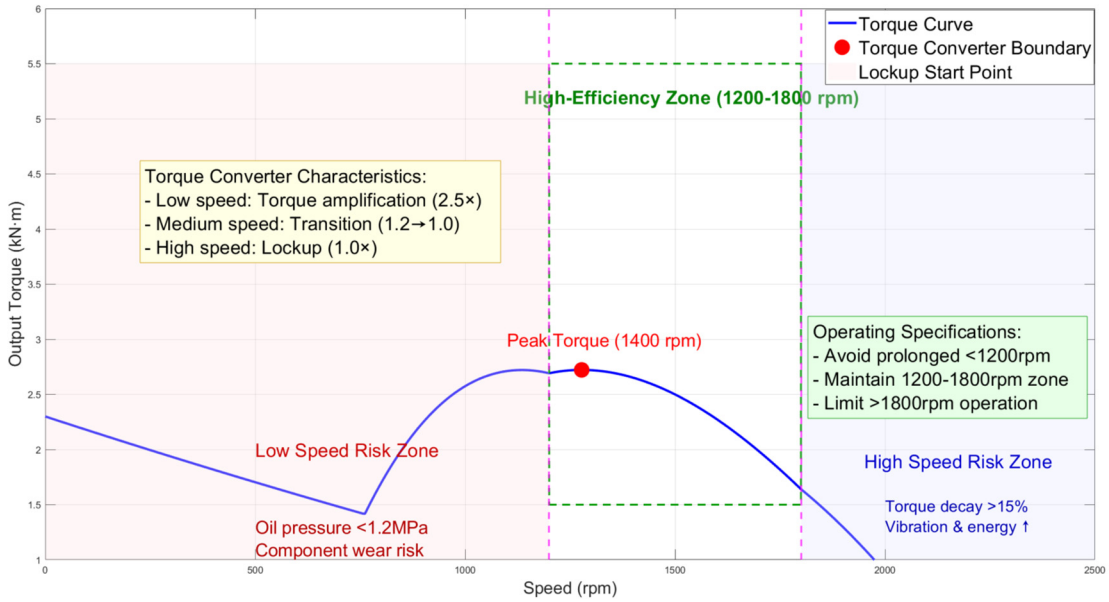

Fig 5. Speed-Torque Characteristic Curve of the Workover Rig

0 clearly illustrates the dynamic influence of rotational speed on output torque. The curve exhibits three distinct stages: In the low-speed range of 0–1200 rpm, the torque amplification effect of the hydraulic torque converter raises the torque to a maximum of 7.0 kN·m (at 600 rpm), while the red risk zone indicates potential wear due to insufficient oil pressure. Within the efficient operating range of 1200–1800 rpm (marked by green dashed lines), the engine delivers a peak torque of 3.0 kN·m at 1400 rpm with optimal mechanical efficiency. Beyond 1800 rpm, torque monotonically decreases after torque converter lock-up (dropping to 2.5 kN·m at 2100 rpm, a 17% reduction), with the blue risk zone highlighting significant vibration and energy consumption increase.

3.4. Torque Spectrum and Resonance Control Analysis

To achieve active control of torque fluctuations, a quantitative analysis of the dynamic parameters of combined downhole motor and shock tool is conducted.

0 based on the rotor-stator interference effect (f = 2.33 Hz), shows a fundamental frequency fluctuation range of 2.26–2.40 Hz and an amplitude variation of ±10%. The amplitude of the second harmonic at 4.66 Hz is 33% of the fundamental amplitude, consistent with the Fourier model An ∝ n^–1.5. When harmonic broadening exceeds 0.3 Hz or the amplitude surpasses the risk threshold of 1.5 kN·m, the system faces the risk of planetary gear fracture. Spectral analysis indicates that adjusting the operating frequency to 2.16 Hz or 2.67 Hz avoids the dangerous resonance band of 2.26–2.40 Hz, reducing the vibration amplitude by 85%, thereby providing a quantitative basis for vibration control.

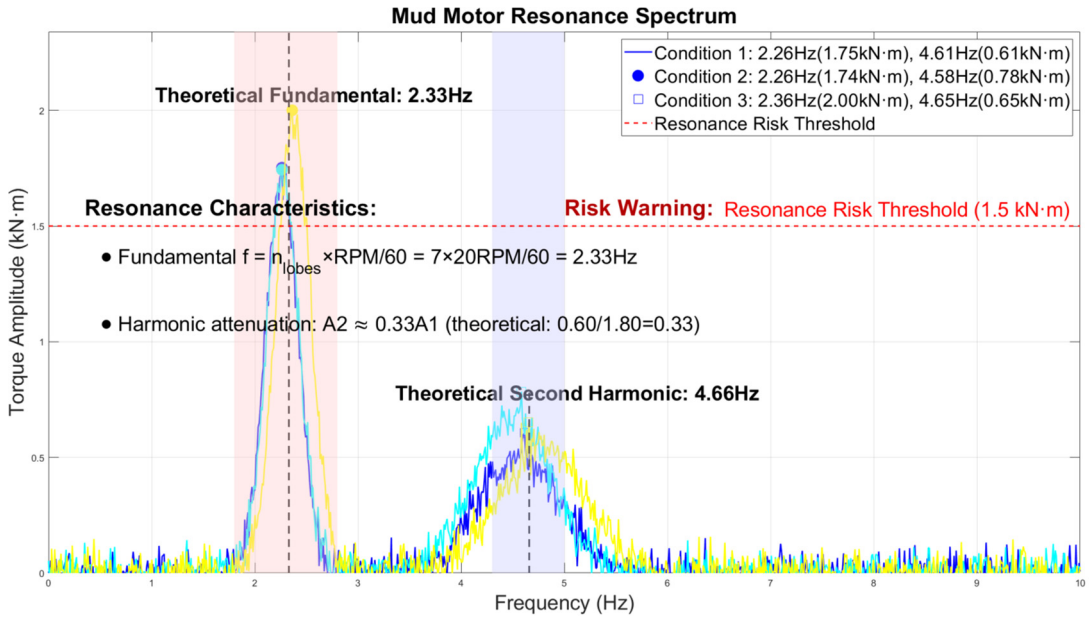

Fig 6. Resonance Spectrum of the Screw Motor

4. CONCLUSION

This study systematically analyzes the static and dynamic characteristics of the workover rig rotary table torque and its influencing factors, clarifying the coupling mechanism among pipe-string friction, mechanical transmission loss, and dynamic inertia in the torque composition. By establishing a torque balance model, it reveals the nonlinear influence of well inclination, dogleg severity, and cuttings bed thickness on frictional torque, and proposes torque suppression strategies based on inclination control, trajectory optimization, and dynamic cuttings management. In terms of mechanical transmission, the attenuation effect of clutch wear on transmission efficiency is quantified, with a wear control threshold of 0.5 mm identified. Comparative analysis of torque response characteristics under different braking modes demonstrates the significant advantage of electromagnetic braking in smoothing torque output and avoiding impact loads.

By quantitatively defining the safety thresholds for key parameters—such as well inclination, dogleg severity, cuttings bed thickness, and clutch wear—this study formulates an operational optimization scheme centered on torque balance, providing direct guidance for the accurate prediction and optimized control of torque in field applications.

DECLARATIONS

All authors declare that they have no conflicts of interest.

REFERENCES

[1] Wang, D., Wu, X., Wang, X., et al. Development and Typical Applications of a Hydraulic While-Drilling Reamer. Mechanical Engineer, 2019, (05): 127-129.

[2] Johancsik C A, Friesen D B, Dawson R. Torque and Drag in Directional Wells-Prediction and Measurement [J]. Journal of Petroleum Technology, 1984, 36(06):987-992. DOI:10.2118/11380-PA.

[3] Burgess, A. (1987) “Designing Well Paths to Reduce Drag and Torque,” SPE Drilling Engineering. Society of Petroleum Engineers (SPE). doi: 10.2118/15463-PA.

[4] Sawaryn, S. J., and J. L. Thorogood. "A Compendium of Directional Calculations Based on the Minimum Curvature Method." SPE Drill & Compl 20 (2005): 24–36. https://doi.org/10.2118/84246-PA.

[5] Payne, M. L., and Fereidoun Abbassian. "Advanced Torque-and-Drag Considerations in Extended-Reach Wells.." SPE Drill & Compl 12 (1997): 55–62. doi: https://doi.org/10.2118/35102-PA.

[6] in, C. Power System Design and Control Strategy for Dual-Power Workover Rigs, Master's thesis, Xi'an Shiyou University. 2022. DOI:10.27400/d.cnki.gxasc.2022.000972.

[7] Miao, J. T. Study on Operational Stability of Drilling Drill String Considering Stochastic Variables. Chemical Engineering & Machinery, (2023). 50(06), 891-895. DOI:10.20031/j.cnki.0254-6094.202306017.

[8] Wang, J. H., Sun, Z. W., Wang, H. F., et al. Analysis of Factors Affecting Friction and Torque in Two-Dimensional Wellbore Trajectory. Drilling & Production Technology, 2016, 39 (04): 12-14+1-2.

[9] Kan-Kan Bai, Mao Sheng, Hong-Bao Zhang, Hong-Hai Fan, Shao-Wei Pan, Real-time drilling torque prediction ahead of the bit with just-in-time learning, Petroleum Science, 2025,430-441, https://doi.org/10.1016/ j.petsci. 2024. 12. 014.

[10] Ngoc Hung- Chu, Hoai Nam- Nguyen, Van Du- Nguyen & Dang Binh- Nguyen (2025) Torque Prediction In Deep Hole Drilling: Artificial Neural Networks Versus Nonlinear Regression Model, Applied Artificial Intelligence, 39:1, 2459482, DOI: 10.1080/08839514.2025.2459482.

[11] Cveticanin, L., Kraljevic, S. & Cverticanin, D. Review on dynamic models of drilling systems applied in oil and gas industry. Acta Mech 234, 4427–4442 (2023). https://doi.org/10.1007/s00707-023-03621-3.

[12] Zhu, J., Zou, D., Li, G., et al. Study on the Mechanism of Friction-Induced Stick-Slip Vibration in Horizontal Well Drill Strings. China Petroleum Machinery, 2021, 49(07): 31-36. DOI:10.16082/j.cnki.issn.1001-4578.2021.07.005.

[13] Liu, D. Research on Common Problems in Logging of High Dogleg Severity Horizontal Wells. Petrochemical Industry Technology, 2019, 26(12): 136-137.

[14] Jabrayilov, Elshan. Friction Reduction by Using Nanoparticles in Oil-Based Mud. 2014. Norwegian University of Science and Technology, PhD dissertation. NTNU Open, http://hdl.handle.net/11250/240487.

[15] Abdullahi Ahmadu."Water-Based Drilling Fluids for High-Temperature Applications and Water-Sensitive and Dispersible Shale Formations." Journal of Petroleum Science and Engineering, Elsevier BV, 2019. https://doi.org/ 10. 1016/j.petrol.2019.01.002.

[16] Guan, Z., Hu, H., Wang, B., et al. Experiment on Rock Breaking Efficiency of PDC Bits Based on Mechanical Specific Energy and Sliding Friction Coefficient. Journal of China University of Petroleum (Edition of Natural Science), 2019, 43(05): 92-100.

[17] Wang, Z., Qin, S. Dynamic Characteristic Analysis of Loader Hydraulic Torque Converter. Journal of South China University of Technology (Natural Science Edition), 2016, 44(07): 41-46.

[18] Zhang, G.; Li, Z.; Wang, Q.; Xu, Z.; Cao, Z. Numerical Investigation of Unsteady Rotor–Stator Interaction Mechanism and Wake Transportation Characteristics in a Compressor with Non-Uniform Tip Clearance Rotor. Energies 2023, 16, 7907. https://doi.org/10.3390/en16237907.